

**This item is the archived peer-reviewed author-version of:**

Neuroplasticity in the cerebello-thalamo-basal ganglia pathway : a longitudinal in vivo MRI study in male songbirds

**Reference:**

Hamaide Julie, Lukacova Kristina, van Audekerke Johan, Verhoye Marleen, Kubikova Lubica, Van Der Linden Anne-Marie.- Neuroplasticity in the cerebello-thalamo-basal ganglia pathway : a longitudinal in vivo MRI study in male songbirds  
Neuroimage - ISSN 1053-8119 - 181(2018), p. 190-202  
Full text (Publisher's DOI): <https://doi.org/10.1016/J.NEUROIMAGE.2018.07.010>  
To cite this reference: <https://hdl.handle.net/10067/1527730151162165141>

Original research paper

## Neuroplasticity in the cerebello-thalamo-basal ganglia pathway: a longitudinal *in vivo* MRI study in male songbirds

### Author names

Julie Hamaide<sup>a\*</sup>, Kristina Lukacova<sup>a, b\*</sup>, Johan Van Audekerke<sup>a</sup>, Marleen Verhoye<sup>a</sup>, Lubica Kubikova<sup>b</sup>, Annemie Van der Linden<sup>a</sup>

\* both authors contributed equally to this work

### Institutional affiliations

<sup>a</sup> Bio-Imaging lab, Department of Biomedical Sciences, University of Antwerp, 2610 Antwerp, Belgium

<sup>b</sup> Centre of Biosciences, Institute of Animal Biochemistry and Genetics, Slovak Academy of Sciences, Bratislava, Slovakia.

### Corresponding authors

#### 1. Prof Dr Annemie Van der Linden

Address: Bio-Imaging Lab, UC 109  
Universiteitsplein 1  
2610 Wilrijk  
Belgium

Telephone number: +32 3 265 27 75

Email address: annemie.vanderlinden@uantwerpen.be

#### 2. Dr Lubica Kubikova

Address: Centre of Biosciences  
Institute of Animal Biochemistry and Genetics, Slovak Academy of Sciences  
Dubravska cesta 9  
840 05 Bratislava  
Slovakia

Telephone number: +421 2 3229 3832

Email address: Lubica.Kubikova@savba.sk

**Declarations of Interests:** None, the authors have no competing interests to declare.

## **ABSTRACT**

Similar to human speech, bird song is controlled by several pathways including a cortico-basal ganglia-thalamo-cortical (C-BG-T-C) loop. Neurotoxic disengagement of the basal ganglia component, i.e. Area X, induces long-term changes in song performance, while most of the lesioned area regenerates within the first months. Importantly however, the timing and spatial extent of structural neuroplastic events potentially affecting other constituents of the C-BG-T-C loop is not clear. We designed a longitudinal MRI study where changes in brain structure were evaluated relative to the time after neurotoxic lesioning or to vocal performance. By acquiring both Diffusion Tensor Imaging and 3-dimensional anatomical scans, we were able to track alterations in respectively intrinsic tissue properties and local volume. Voxel-based statistical analyses revealed structural remodeling remote to the lesion, i.e. in the thalamus and, surprisingly, the cerebellum, both peaking within the first two months after lesioning Area X. Voxel-wise correlations between song performance and MRI parameters uncovered intriguing brain-behavior relationships in several brain areas pertaining to the C-BG-T-C loop supervising vocal motor control. Our results clearly point to structural neuroplasticity in the cerebellum induced by basal ganglia (striatal) damage and might point to the existence of a human-like cerebello-thalamic-basal ganglia pathway capable of modifying vocal motor output.

## **Keywords**

Basal ganglia, DTI, MRI, songbird, vocal motor production

## **Abbreviations (not standard to the field)**

AFP	anterior forebrain pathway
C-BG-T-C	cortico-basal ganglia-thalamo-cortical
DLM	dorsolateral nucleus of the medial part of the anterior thalamus
HVC	abbreviation used as a proper name (high vocal center)
LMAN	lateral magnocellular nucleus of the anterior nidopallium
PMP	posterior motor pathway
RA	robust nucleus of the arcopallium
ROI	region-of-interest
SAP	sound analysis pro

## 1 1 INTRODUCTION

2 While nearly all vertebrate species are able to vocalize, only few species, including humans and  
3 songbirds, communicate through acoustically complex socially-learned vocalizations (Petkov and  
4 Jarvis 2012; Jarvis 2004). Both speech and song are highly complex and rapid learned motor  
5 behaviors, driven by a sharply tuned vocal motor apparatus that enables adaptation of the temporal  
6 and spectral content of sounds to result in complex communication signals. Based on molecular  
7 genetics, neurophysiology and behavioral studies, songbirds –especially zebra finches– are currently  
8 regarded as a valuable model to study aspects of human speech learning in a laboratory setting  
9 (Brainard and Doupe 2013; Bolhuis, Okanoya, and Scharff 2010). Opposed to humans, zebra finches  
10 learn to produce only one song which will remain unchanged throughout their life in normal  
11 circumstances, and, importantly, only male zebra finches sing. This behavioral dimorphism is  
12 reflected in the neural substrate supporting vocal motor behavior as the volume of several song  
13 control nuclei is significantly larger in male compared to female zebra finches (Nottebohm and  
14 Arnold 1976; MacDougall-Shackleton and Ball 1999).

15 Despite fundamental differences in the overall organization between the songbird and human brain,  
16 convincing parallels exist in the brain networks supporting acquired vocal behavior (Jarvis et al.  
17 2005). Like human speech, bird song production relies on cortical areas (Wild 1997) and on a cortico-  
18 basal ganglia-thalamo-cortical (C-BG-T-C) loop (Figure 1-A). This loop enables trial-and-error vocal  
19 exploration during vocal learning and contributes to song maintenance in adulthood (Nordeen and  
20 Nordeen 2010; Brainard 2004; Scharff and Nottebohm 1991). In songbirds, the cortical pathway  
21 directly responsible for the motor aspect of song production is termed the posterior motor pathway  
22 (PMP) and consists of a direct connection between premotor nucleus HVC (abbreviation used as a  
23 proper name; (Reiner, Perkel, et al. 2004); Figure 1-A) and the robust nucleus of the arcopallium  
24 (RA), avian analogue of the mammalian (laryngeal) motor cortex (Pfenning et al. 2014). RA ultimately  
25 connects to brain stem nuclei that innervate the vocal motor neurons (Vicario 1991) and respiratory  
26 centers (Wild 1993). The C-BG-T-C loop or anterior forebrain pathway (AFP) originates in HVC from  
27 where it projects to Area X, a large brain region that is functionally and structurally similar to the  
28 mammalian basal ganglia and contains striatal- and pallidal-like neurons (Person et al. 2008; Reiner,  
29 Laverghetta, et al. 2004). The pallidal neurons of Area X course to the dorsolateral nucleus of the  
30 medial part of the anterior thalamus (DLM), which in turn sends projections to the lateral  
31 magnocellular nucleus of the anterior nidopallium (LMAN), a frontal cortical nucleus. Lastly, LMAN  
32 sends recurrent projections directly to Area X and an axon collateral to the final target of the AFP,  
33 nucleus RA (Nixdorf-Bergweiler, Lips, and Heinemann 1995; Vates and Nottebohm 1995). Compelling  
34 evidence suggests similarity between the cortical areas HVC and LMAN and Broca’s area in humans

35 (Jarvis 2004; Pfenning et al. 2014; Moorman et al. 2012). In humans, a second subcortical pathway  
36 has been identified that supports an important role in vocal learning and vocal motor control, i.e. the  
37 cerebro-cerebellar motor loop (Ziegler and Ackermann 2017). To date, only limited evidence points  
38 towards a functionally similar avian counterpart, i.e. where Area X receives input from the  
39 cerebellum through the thalamus (Person et al. 2008; Doupe et al. 2005).

40 Both in humans and songbirds, new-born neurons migrate to the striatum in normal circumstances  
41 (Goldman and Nottebohm 1983; Doetsch and Scharff 2001; Kosubek-Langer, Schulze, and Scharff  
42 2017; Ernst et al.). Disruption of the C-BG-T-C loop in adult songbirds, by neurotoxic or electrolytic  
43 lesioning of Area X, does not affect the overall structure of their song (Scharff and Nottebohm 1991),  
44 but is capable of inducing alterations to song tempo or transient stuttering-like song (Kubikova et al.  
45 2014; Kobayashi, Uno, and Okanoya 2001). The change in behavior is mirrored by a massive  
46 upregulation of proliferation and migration of progenitor cells in and near the lesioned area  
47 (Kubikova et al. 2014). Structural and functional neuroplastic changes have been described along the  
48 C-BG-T-C loop, including the loss of Area X-originating DLM axonal terminal fields throughout the  
49 first 3-4 days after neurotoxic lesion (Luo and Perkel 1999; Kubikova, Turner, and Jarvis 2007), and  
50 altered singing-induced gene expression in the downstream motor cortex region RA, the final target  
51 of the AFP (Kubikova et al. 2014). Together, these data suggest that neurotoxic disengagement of  
52 one song control system component affects the other constituents of the same circuitry and results  
53 in aberrant vocal motor performance. However, several questions still remain unanswered. Do  
54 structural alterations induced by the neurotoxic lesioning extend beyond DLM, the first downstream  
55 target of Area X, propagate upstream to the cortical premotor area HVC or maybe even affect  
56 remote areas that are not part of the song control system? Can we establish brain-behavior  
57 relationships between the structural micro-architecture of specific anatomical areas and song  
58 performance?

59 We sought to address these questions by designing a longitudinal study using *in vivo* Magnetic  
60 Resonance Imaging tools that can repeatedly map the structural architecture of the entire zebra  
61 finch brain before and after Area X lesioning (Figure 1-B). More specifically, we employed a recently  
62 optimized *in vivo* Diffusion Tensor Imaging protocol (Hamaide et al. 2017) combined with 3-  
63 dimensional (3D) T2-weighted anatomical scans. The 3D anatomical scans were processed for  
64 automated morphometric analyses (termed tensor- or deformation-based morphometry (DBM);  
65 (Ashburner and Ridgway 2015)) that provide a quantitative readout for localized relative volume  
66 changes. The DTI data inform on possible changes in microstructural tissue properties deduced from  
67 alterations in the local diffusion profiles of water molecules within a voxel (Mori and Zhang 2006).  
68 We found that in addition to previously documented neuroplastic events in the thalamus,

69 surprisingly, also the lateral cerebellar nuclei display structural adaptations occurring within the first  
70 two months after Area X lesioning. We further observed clear relationships between song motif  
71 length and several components of the C-GB-T-C loop. More generally, our findings suggest the  
72 existence of a cerebellar-thalamo-basal ganglia pathway that might be capable of modulating vocal  
73 motor production similar to the feedforward cerebro-cerebellar pathway described in humans.

## 74 **2 MATERIALS AND METHODS**

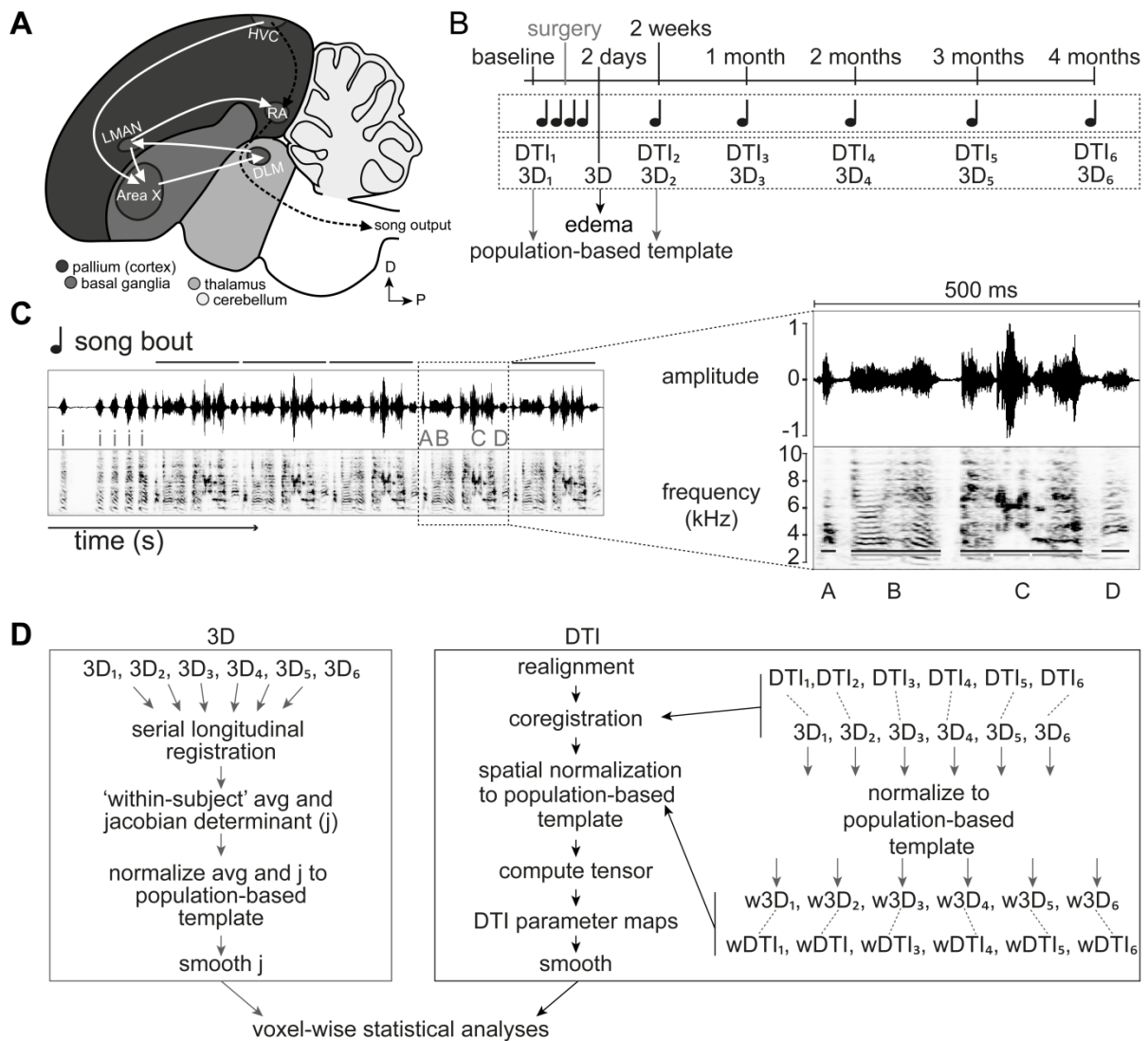
### 75 **2.1 Animals**

76 Adult male zebra finches (*Taeniopygia guttata*; n=14; age > 200 days *post* hatching (dph)) bred in the  
77 animal facility of the Slovak Academy of Sciences or the University of Antwerp, participated to the  
78 study. We did not include female zebra finches as only males sing (MacDougall-Shackleton and Ball  
79 1999). Except during the song recordings, the birds were group-housed in large indoor aviaries, on a  
80 12h/12h light/dark cycle with food and water available *ad libitum* at all times. All experimental  
81 procedures were reviewed and approved by the State Veterinary and Food Administration of the  
82 Slovak Republic (permit number: 3569/16-221) and the Committee of Animal Care and Use at the  
83 University of Antwerp, Belgium (permit number: 2015-03).

### 84 **2.2 Study design**

85 A detailed overview of the study design can be found in Figure 1-B. The neurotoxic lesion consisted  
86 of a stereotaxic injection of ibotenic acid in Area X of both hemispheres. This neurotoxic compound  
87 causes neural cell death by over-excitation, while keeping the surrounding tissue –extracellular  
88 matrix and passing nerve terminals from extrinsic origin– unaffected (Schwarcz et al. 1979). Since T2-  
89 weighted MRI images are used to locate edema in the brain, we verified the location of the lesion  
90 based on a hyper-intense (bright) signal indicative of edema, 2 days after surgery. Following each MR  
91 experiment, the songs of the birds were recorded and analyzed.

92 MRI data, i.e. DTI and 3D scans, were acquired before and at five time points after introducing a  
93 neurotoxic lesion in Area X, i.e. 2 weeks, 1 month, 2 months, 3 months and 4 months after surgery.  
94 All MRI data were prepared for voxel-wise statistical testing which enables unbiased data-based  
95 detection of areas that display structural changes in the entire brain without *a priori* selection of  
96 Regions-of-Interest (ROIs). We designed voxel-wise statistical tests that inform on potential changes  
97 in tissue volume (3D) or intrinsic properties (DTI) over time or that explore potential correlations  
98 between song performance and the structural properties of the zebra finch brain.



99

**Figure 1:** Schematic view of the song control system in songbirds (A), the study design (B) and the processing of the song (C) and MRI (D) data. The schematic songbird brain (A) presents two main pathways in control of song, i.e. cortical pathway that directly connects HVC and RA (black dashed arrows), and an indirect C-BG-T-C loop that sequentially connects HVC-Area X-DLM-LMAN-RA (solid white arrows). The darkest grey area refers to the avian pallium, similar to the mammalian cortex. Dark grey covers the avian striatum and pallidum, similar to the mammalian basal ganglia. Light grey areas refer to the thalamic zone and cerebellum. The arrows in the bottom right corner refer to dorsal (D) and posterior (P). More details on the study design (B) and MRI data processing (D) can be found in sections 2.2 and 2.6 respectively. Male zebra finches usually sing song bouts (C) consisting of introductory notes (i) followed by several renditions of the song motif (indicated by horizontal lines above the song bout). Each motif consists, on average, of 3-5 syllables (indicated by the black lines and letters below the inset, e.g. A-B-C-D) that can be further subdivided into notes (indicated by grey lines), e.g. syllable C consists of 3 notes. All song analyses have been performed on sound spectrograms (frequency) and included measurements of the motif, syllable and inter-syllable interval duration.

### 100 2.3 Stereotactic surgery

101 The induction of the bilateral neurotoxic lesion was performed similar to previously described  
 102 protocols (Kubikova et al. 2014; Lukacova et al. 2017; Lukacova et al. 2016). In brief, the birds were

103 anaesthetized by inhalation of isoflurane in a mixture of oxygen and nitrogen (induction: 2.5 %;  
104 maintenance: 1.5-2.5 %; IsoFlo®, Abbott, Illinois, USA). After localizing the zero-point, i.e. a  
105 midsagittal landmark that defines the transition between the cerebrum and the cerebellum, we  
106 navigated a glass micropipette to the center of Area X at the following coordinates: 4.5-5 mm rostral,  
107 1.3 mm lateral (to both left and right hemisphere) and 3.5 mm ventral. The head was placed at a 25°  
108 angle so as to prevent traversing LMAN while inserting the needle. Each Area X received three  
109 injections of 46 µl ibotenic acid (total volume 138 µl per hemisphere; 1%; pH 7.3-7.6; Tocris  
110 Bioscience UK), administered approximately 2 min apart using the Nanoject II injector (Drummond  
111 Scientific, USA). After the last injection, the needle was left in place for approximately 5 min to  
112 minimize possible back-flow along the path of the needle, after which the injector was retracted  
113 gently. When all injections were successfully performed, the skin was glued together and mesocaine  
114 gel was applied. All birds were monitored until full recovery.

#### 115 **2.4 Song recordings and analyses**

116 The songs of the birds were recorded in sound attenuating chambers via the automated song  
117 detection setup implemented in Sound Analysis Pro (SAP) software version 2011.104  
118 ((Tchernichovski et al. 2000); <http://soundanalysispro.com/>). Only during song recordings, the birds  
119 were housed solitary and all recordings contain exclusively undirected songs (not directed to a  
120 female zebra finch). As song tempo changes over the course of a day (Glaze and Troyer 2006), we  
121 examined the first 25 song motifs sung after initiation of the photophase. To be able to compare the  
122 song tempo, only the same sequence of syllables within a motif in the same bird were selected for  
123 the analyses, i.e. only motifs containing the same number of syllables (ABCD) were measured even if  
124 the bird sometimes sang a syllable more (ABCDE) or less (ABC; Figure 1-C). Introductory notes and  
125 calls were omitted from all analyses. First, motif duration was quantified, defined by respectively the  
126 duration of one song motif visible on the sound spectrogram. Next, individual syllables were  
127 segmented based on sharp changes in amplitude and Wiener entropy visible on the sound  
128 spectrogram and the duration of the syllables and inter-syllable intervals, i.e. time period in between  
129 two consecutive syllables, was measured.

130 To investigate whether certain syllable types respond differently after surgery, two independent  
131 researchers categorized each syllable based on visual inspection of the sound spectrograms obtained  
132 at baseline. Syllable categorisation was performed in accordance with criteria defined by Sturdy et  
133 al. (Sturdy, Phillmore, and Weisman 1999), and included short slide notes, high notes, flat notes,  
134 slide notes, combination notes, unclassified notes, and unreadable notes.

## 135 **2.5 MRI data acquisition**

136 All MRI experiments were executed on a 7T horizontal small animal scanner (PharmaScan 70/16 US,  
137 Bruker BioSpin GmbH, Germany), equipped with the standard setup including a quadrature transmit  
138 volume coil, a linear array coil designed for mice and a 400 mT/m gradient insert (Bruker BioSpin,  
139 Germany). To minimize stress and movement during acquisition, the birds were anaesthetized with  
140 isoflurane in a mixture of oxygen and nitrogen (induction: 2.5%; maintenance: 1.3-1.7%; IsoFlo®,  
141 Abbott, Illinois, USA). Throughout the entire imaging session, the bird's breathing rate was  
142 monitored using a pressure-sensitive pad positioned under the chest of the animals, and body  
143 temperature was maintained within narrow physiological levels ( $40.0 \pm 0.2^\circ\text{C}$ ) by means of a cloacal  
144 thermistor probe connected to a warm-air feedback system (SA instruments, Inc.). To enable  
145 consistent head positioning over different imaging sessions, the birds were placed in an MR-  
146 compatible, custom-build stereotactic scanner bed.

147 After obtaining pilot scans, a field map was acquired to measure local inhomogeneities in the  
148 magnetic field which aided subsequent local shimming procedures. Next, the DTI data were  
149 collected using a diffusion-weighted spin echo (SE) echo planar imaging (EPI) pulse sequence with  
150 the following imaging parameters: TE 22 ms, TR 7000 ms, FOV (20x15) mm<sup>2</sup>, acquisition matrix  
151 (105x79), in-plane resolution (0.19x0.19) mm<sup>2</sup>, slice thickness 0.24 mm, 28 horizontal slices, b-value  
152 670 s/mm<sup>2</sup>, diffusion gradient duration ( $\delta$ ) 4 ms, diffusion gradient separation ( $\Delta$ ) 12 ms. A total of  
153 21  $b_0$  images and 60 unique diffusion gradient directions were sampled ~~in three scans each~~  
154 ~~containing 7  $b_0$  and 20 diffusion weighted volumes~~. This entire DTI protocol was repeated twice to  
155 ~~increase the signal-to-noise ratio~~ (total DTI acquisition duration: approximately 72 min). Immediately  
156 after the DTI scan, a T<sub>2</sub>-weighted 3D Rapid Acquisition with Relaxation Enhancement (RARE) scan  
157 was acquired with the following characteristics: TE 11 ms (TE<sub>eff</sub> 55 ms), TR 2500 ms, RARE factor 8,  
158 FOV (18x16x10) mm<sup>3</sup>, matrix (256x92x64) zero-filled to (256x228x142), spatial resolution  
159 (0.07x0.17x0.16) mm<sup>3</sup> zero-filled to (0.07x0.07x0.07) mm<sup>3</sup>, scan duration 29 min. The FOV of the 3D  
160 RARE scans covered the entire birdbrain.

## 161 **2.6 MRI data processing**

162 All MRI data was prepared for voxel-wise statistical analyses using SPM12 (Statistical Parametric  
163 Mapping, version 6225, <http://www.fil.ion.ucl.ac.uk/spm/>) complemented with the Diffusion II and  
164 Dartel (Ashburner 2007; Ashburner and Friston 2009) toolboxes, and the Advanced Normalization  
165 Tools (ANTs; <http://stnava.github.io/ANTs/>; (Avants et al. 2011)). An overview of the different steps  
166 of the DBM and DTI processing pipelines is included in Figure 1-D.

### 167 **2.6.1 Population-based template**

168 First, we created a population-based template based on all 3D anatomical scans acquired at baseline  
169 and at 2 weeks *post-surgery* using the ‘atlasbuildtemplate’ function in ANTs (Avants et al. 2011;  
170 Avants et al. 2010; Avants et al. 2008). The resulting inter-subject template was used as reference  
171 space for the voxel-wise DBM and DTI analyses. Important to note is that no visible traces of edema  
172 could be observed in the 3D RARE scans obtained 2 weeks *post-surgery*. In contrast, only very small  
173 hypo-intensities covering the path taken by the needle and the core of the lesion were discernible.

### 174 **2.6.2 Deformation-Based Morphometry (DBM)**

175 For each animal, an average 3D RARE (‘within-subject template’ or ‘midpoint average’) was  
176 estimated based on the 3D RARE images acquired before and at five time points after introducing a  
177 neurotoxic lesion in Area X, i.e. 2 weeks, 1 month, 2 months, 3 months, and 4 months after surgery  
178 (Figure 1-B), using the serial longitudinal registration tool (SLR; (Ashburner and Ridgway 2012))  
179 embedded in SPM12. This step includes an intensity inhomogeneity (bias field) correction followed  
180 by a rigid-body transformation combined with symmetric non-linear diffeomorphic mapping. Next,  
181 the resulting midpoint average was masked, by manual delineation in Amira (v5.4.0, FEI;  
182 <https://www.fei.com/software/amira-3d-for-life-sciences/>), to exclude non-brain tissue and spatially  
183 normalized to the population-based template built in ANTs using the ‘oldNormalise’ function in SPM.  
184 The latter incorporates a global affine transformation followed by nonlinear deformations. The  
185 transformation matrix estimated by this step was applied to the jacobian determinant maps –  
186 without modulation, which would account for between-subject volume differences– outputted by  
187 the SLR step. For multiple regression analyses, the normalized jacobian determinant maps were log-  
188 transformed. Lastly, all normalized jacobian determinant maps were smoothed *in-plane* using a  
189 Gaussian filter with FWHM set at (0.28x0.28x0.28) mm<sup>2</sup>.

### 190 **2.6.3 Diffusion Tensor Imaging (DTI)**

191 After assigning the b-value and diffusion gradient directions pertaining to each volume, the DTI scans  
192 were realigned to the first volume by a two-step procedure. Firstly, an initial estimation of  
193 movement was performed on the  $b_0$  images, after which a second movement estimate included all  
194 data i.e.  $b_0$  and diffusion weighted scans. Next, the realigned diffusion time series were co-registered  
195 to the 3D RARE scan acquired at the same time-point (rigid inter-modal within-bird spatial  
196 registration), using normalized mutual information as objective function. In parallel, the masks  
197 delineated on the midpoint average produced by the SLR step, were back-projected to the native  
198 space of the individual datasets using the inverse of the deformation fields computed by the SLR.  
199 Next, the masked individual 3D RAREs acquired at each time point were bias corrected and spatially  
200 normalized to the population-based template using the oldNormalise function in SPM12 (non-linear

201 between-bird spatial transformation). Then, the spatial normalization parameters estimated on the  
202 masked, bias corrected 3D RARE scans were applied to the diffusion time series and the diffusion  
203 time series was up-sampled to an isotropic resolution of 0.19 mm. In parallel, the diffusion vectors  
204 were updated to account for potential (linear) rotations incurred by the realignment, co-registration  
205 and normalization procedures using the 'copy and reorient diffusion information' tool of the  
206 Diffusion II toolbox. The normalized diffusion data were used to estimate the diffusion tensor. Via  
207 decomposition of the diffusion tensor one obtains its real Eigenvectors ( $e_1, e_2, e_3$ ) and Eigenvalues  
208 ( $\lambda_1, \lambda_2, \lambda_3$ ), which represent the principle axes and the corresponding radii of the 3D diffusion  
209 ellipsoid. The direction of the principal Eigenvector estimates the main diffusion direction, which is  
210 for example the direction parallel to the axonal tracts in the brain white matter. Based on the  
211 Eigenvalues, other diffusion metrics are calculated for each voxel in the image: Mean Diffusivity  
212 (MD) is the average of the three Eigenvalues; and Fractional Anisotropy (FA) which ranges from '0' to  
213 '1' indicates the anisotropy of the diffusion profile where CSF is characterized by low FA and high  
214 MD, white matter by high FA (Mori and Zhang 2006). Finally, the DTI parameter maps were  
215 smoothed in plane with a Gaussian kernel of (0.38x0.38) mm<sup>2</sup>.

## 216 2.7 Statistical analyses

217 All voxel-wise statistical tests were performed in SPM12, while statistical analyses on the song data  
218 and cluster-based region-of-interest (ROI) data were executed in JMP® (Version 13, SAS Institute  
219 Inc., Cary, NC, 1989-2007) and rmcrr (Bakdash and Marusich 2017) software.

### 220 2.7.1 Song analyses

221 We tested whether the motif, syllable or inter-syllable duration changed significantly over time using  
222 linear mixed models ('time point' as fixed effect, 'subject' as random effect, 'subject\*timepoint' as  
223 random slope, and syllable-identity was nested within subject for analyses on the syllable and inter-  
224 syllable intervals) and selected Tukey's Honest Significant Difference (HSD) for *post hoc* testing.  
225 Statistical analyses were performed on absolute (averaged) song scores, but presented as data  
226 normalized to the baseline level.

### 227 2.7.2 Voxel-based analyses

228 We executed voxel-wise repeated-measures ANOVAs' and voxel-wise multiple regressions on each  
229 set of MRI parameter map separately (FA, MD, 1, 2, 3, (log) jacobian determinant) to uncover which  
230 brain areas display a significant change in MRI parameter over time or exhibit a significant  
231 correlation between motif scores and MRI parameters. Only clusters surviving a Family-Wise-Error  
232 (FWE) correction for multiple comparisons set at  $p < 0.05$ , and containing at least ( $k_{\epsilon}$ ) 80 voxels or 10  
233 voxels for respectively the DBM and DTI analyses, were considered significant.

234 Time-dependent changes of the structural properties of the brain were evaluated by setting up a  
235 voxel-wise repeated-measures ANOVA in a flexible factorial design for each smoothed MRI  
236 parameter map separately, with 'time point' as fixed factor and 'subject' as random factor. Next,  
237 clusters covering a similar anatomical area in both hemispheres were converted to ROIs ('cluster-  
238 based ROIs'). Next, we extracted the average MRI parameters for each cluster-based ROI and  
239 performed a mixed model with time point as fixed factor and bird-identity as random factor,  
240 combined with *post hoc* Tukeys' HSD tests to situate when in time difference in MRI parameters  
241 occurred.

242 The voxel-wise multiple regressions tested for potential positive or negative correlations between  
243 each set of MRI parameters and motif score, including datasets obtained at all 6 time points.  
244 Clusters that displayed a significant correlation between a particular MRI parameter and song  
245 feature were converted to ROIs of which the average MRI parameter was extracted and Spearmans'  
246  $\rho$  was selected to explore the nature and strength of the overall association between the MRI  
247 parameters and song feature scores. To discriminate whether the correlation was mainly due to  
248 within-bird variance, we performed a repeated-measures correlation using the custom-build R-script  
249 'rmcorr' developed by (Bakdash and Marusich 2017).

## 250 **3 RESULTS**

### 251 **3.1 *In vivo* assessment of the spatial extent of the lesion**

252 Two days after neurotoxic injury, we acquired T2-weighted 3D anatomical scans to assess the spatial  
253 extent of the lesion based on hyper-intense voxels indicative of edema. The edema might either be  
254 induced by mechanical damage, e.g. along the path of the needle, or by neurotoxic injury at the  
255 injection site. Based on these scans, we concluded that 12 out of 14 birds displayed a hyper-intense  
256 signal co-localized with major parts of Area X (Figure 2-A). The 2 birds that did not show a lesion in  
257 the right anatomical area were excluded from further analyses. Furthermore, besides the target  
258 area, hyper-intense voxels were observed near the rostral border of the most medial part of  
259 LMAN<sub>core/shell</sub> (Figure 2-B). MMAN, situated closer to the midline, was not covered by hyper-intense  
260 signals and thus not likely to be affected by the surgical procedure.

261 Next, the scans obtained two days after surgery were spatially normalized to the population-based  
262 template and averaged into one 3D image. This dataset was used to delineate the 'average' region  
263 affected by edema. The delineation was projected onto the population-based template and  
264 indicated by means of a black area (Figure 2, bottom rows). This dataset serves as an anatomical  
265 reference underlying all statistical parametric maps.

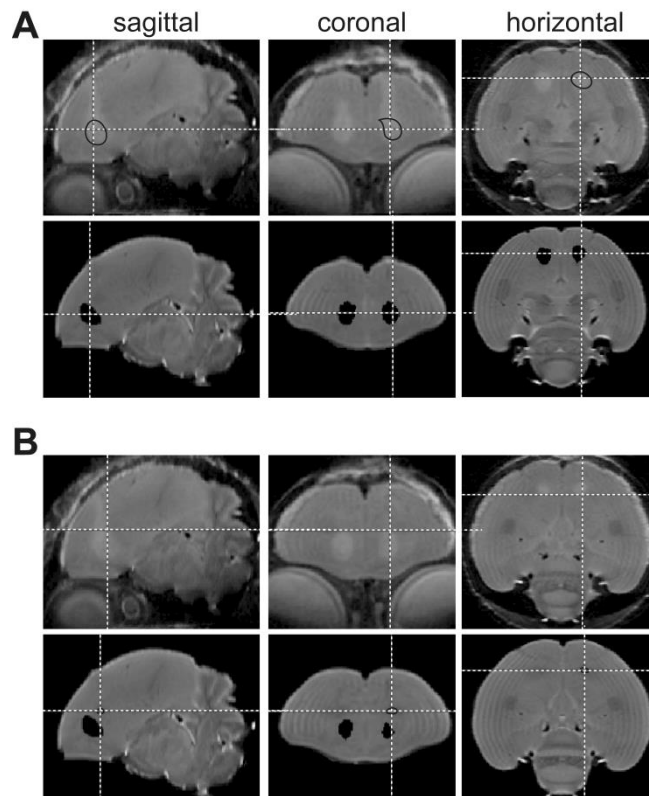


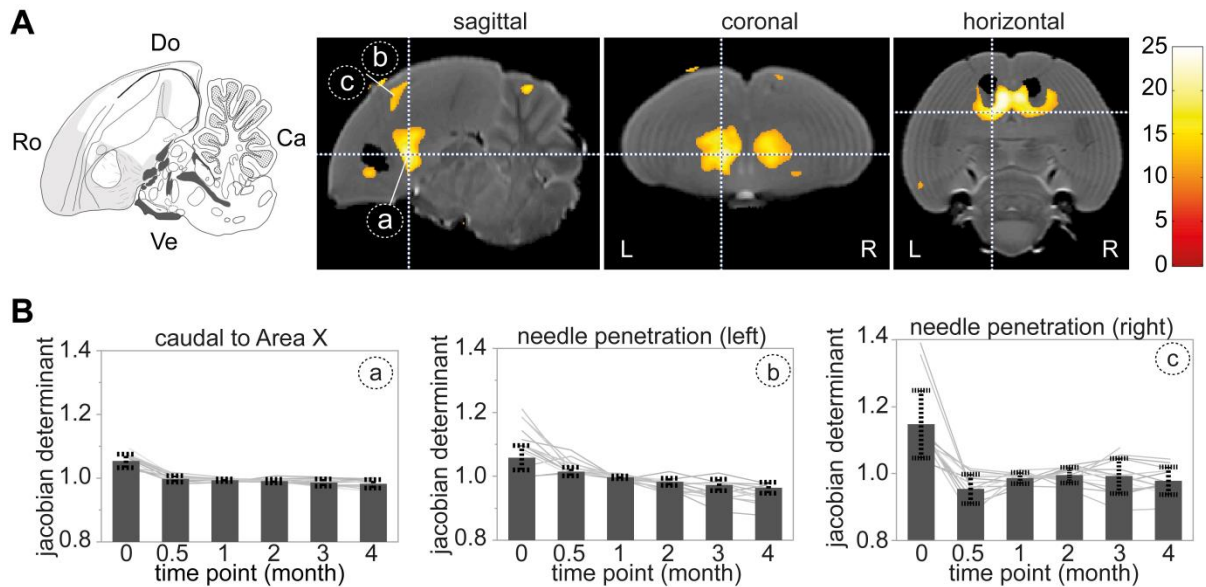
**Figure 2:** T2-weighted 3D RARE scans obtained two days after surgery inform on the spatial extent of the lesion. The crosshairs point to Area X (A) or LMAN (B), both are delineated by a black line in one hemisphere and visible as respectively hyper- (edema) or hypo-intense (intrinsic MRI contrast) area on the contralateral side. The top row of (A) and (B) display the average 3D based on all 3D RARE scans obtained 2 days after surgery (n=12). Areas affected by edema induced by either neurochemical (ibotenic acid) or mechanical (needle) damage are represented by hyper-intense (bright) voxels. The bottom rows of (A) and (B) illustrate the population-based template where the manually delineated black colored regions refer to the parts of the striatum (Area X) affected by edema. The delineation is based on the hyper-intense area visible in the top row and only contains voxels above a manually defined voxel-intensity threshold (retain only brightest voxels).

266

### 267 3.2 DBM exposes relative volume changes in the striatum

268 The voxel-wise repeated measures ANOVA (n=12) of the smoothed non-modulated jacobian  
 269 determinant maps identified a main effect of time in a large bilateral cluster covering the caudal,  
 270 medial, and lateral surroundings of the lesion (Figure 3-A, cluster (a); the cluster ( $p_{FWE}<0.001$   
 271  $k_E=25359$ ) includes 3 main peaks: peak 1  $p_{FWE}<0.001$   $F=24.82$ ; peak 2:  $p_{FWE}<0.001$   $F=6.84$ ; peak 3:  
 272  $p_{FWE}<0.001$   $F=18.96$ ). Interestingly, the cluster did not co-localize with the dark area that reflects the  
 273 lesioned region. It appears to be situated mainly in the striatum and exceeds ventrally to the ventral  
 274 pallidum and dorsally to the nidopallium (cortical-like region). Furthermore, several smaller clusters  
 275 were found where the needle entered the brain, dorsal to Area X, (Figure 3-A, clusters (b) and (c);  
 276 left: cluster level  $p_{FWE}<0.001$   $k_E=307$ ; peak level  $p_{FWE}<0.001$   $F=18.83$ ; right cluster<sub>1</sub>: cluster level  
 277  $p_{FWE}<0.001$   $k_E=350$ ; peak level  $p_{FWE}<0.001$   $F=20.10$ ; right cluster<sub>2</sub>: cluster level  $p_{FWE}<0.001$   $k_E=671$ ;  
 278 peak level  $p_{FWE}<0.001$   $F=16.00$ ). Voxel-wise tests assessing differences between consecutive time

279 points (data not shown) informed that the main effect of time is caused by differences between  
 280 baseline and 2 weeks *post*-surgery. This trend is visualized in Figure 3-B which plots the average  
 281 jacobian determinant for the cluster-based ROIs at each individual time point (relative volume of the  
 282 cluster is larger at baseline ( $j > 1$ ), compared to at 2 weeks *post*-surgery ( $j \approx 1$ )).



283

**Figure 3: DBM analysis reveals relative volume changes in the striatum.** **A:** The statistical parametric maps represent the results of a main effect of time derived from a repeated-measures ANOVA ( $n=12$ ) on the jacobian determinant maps. The atlas drawing on the left –obtained from the zebra finch histological atlas browser (Oregon Health & Science University, Portland, OR 97239; <http://www.zebrafinchatlas.org> (Karten et al. 2013)– was taken at approximately the same lateral position as the sagittal MR image immediately adjacent to it. The crosshairs in the sagittal slice indicate the relative location of the coronal and horizontal MR slices displayed on the right. Results are overlaid on the population-based template and scaled according to the color-code on the right (F values). Only voxels that reached  $p_{FWE} < 0.05$  and took part of a cluster of  $k_E \geq 80$  contiguous voxels are displayed. The black area reflects the area affected by the surgery (ibotenic acid) and was drawn based on the 3D RARE scans acquired two days after surgery. **B:** The bar graphs illustrate the mean  $\pm$  standard deviation of the mean jacobian determinant of the clusters identified in A (denoted with encircled letter). The grey lines refer to the evolution of the average jacobian determinant in a specific cluster-based ROI for each individual animal. The different cluster-based ROIs overlay with (a) the medial striatum caudal to the lesion site, and (b-c) the needle penetration areas in respectively the left and right hemispheres. Time point ‘0’ refers to the baseline, before neurotoxic lesioning. Abbreviations: Do: dorsal; Ve: ventral; Ro: rostral; Ca: caudal; L: left; R: right.

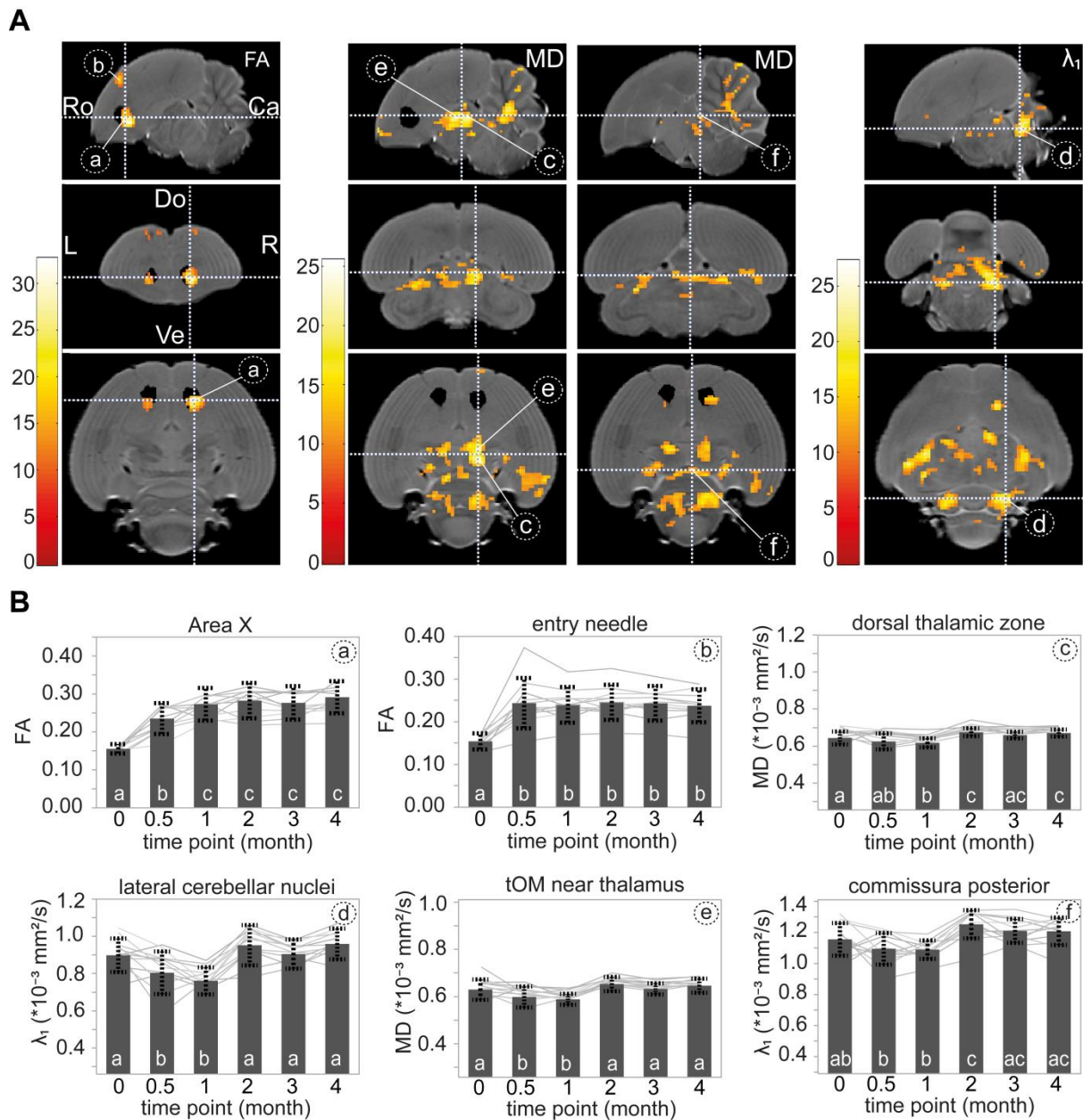
### 284 3.3 DTI uncovers lesion-induced structural remodeling of the cerebello-thalamo-striatal 285 pathway within the first two months after a neurotoxic lesion

286 The voxel-wise repeated-measures ANOVA ( $n=12$ ) identified large widespread bilateral clusters  
 287 displaying a main effect of time in FA, MD and  $\lambda_1$  (Figure 4-A). In contrast, clusters found in the  
 288 smoothed  $\lambda_2$  and  $\lambda_3$  maps did not appear bilateral and were therefore not further explored. When  
 289 inspecting differences in FA over time, a very clear bilateral cluster was observed near the striatum  
 290 and Area X, partly invading the lesion (Figure 4-A, cluster (a); left: cluster level:  $p_{FWE} < 0.001$   $k_E = 97$ ;

291 peak voxel:  $p_{FWE}<0.001$ ;  $F=32.54$ ; right: cluster level:  $p_{FWE}<0.001$   $k_E=40$ ; peak voxel:  $p_{FWE}<0.001$ ;  
292  $F=19.84$ ). Another cluster was found dorsal to Area X, spatially corresponding with the entrance of  
293 the needle in the brain (Figure 4-A, cluster (b); left: cluster level:  $p_{FWE}$   $k_E=80$ ; peak level:  $p_{FWE}<0.001$ ;  
294  $F=22.50$ ; right: cluster level  $p_{FWE}<0.001$   $k_E=51$ ; peak level:  $p_{FWE}<0.001$   $F=16.62$ ). No further changes in  
295 FA were found. A similar cluster covering Area X was present when testing  $\lambda_1$  over time (not shown;  
296 left: cluster level:  $p_{FWE}<0.001$   $k_E=29$ ; peak level:  $p_{FWE}<0.001$   $F=17.96$ ; right: cluster level  $p_{FWE}<0.001$   
297  $k_E=78$ ; peak level:  $p_{FWE}<0.001$ ;  $F=20.44$ ). Furthermore, a widespread cluster covering caudal  
298 subpallial (i.e. subcortical) parts of the telencephalon and extending ventrally towards the  
299 mesencephalon and cerebellum was also found to display changes in  $\lambda_1$  and MD over time. Several  
300 sub-peaks of this large cluster could be anatomically identified, including the dorsal thalamic zone  
301 (including DLM; Figure 4-A, cluster (c)), an anatomically discrete bilateral cluster in the lateral  
302 cerebellar nuclei (Figure 4-A, cluster (d)), the medial parts of the *tractus occipitomesencephalicus*  
303 (tOM: Figure 4-A, cluster (e)), and the *commissura posterior* (Figure 4-A, cluster (f)).

304 Next, the clusters were converted to ROIs of which the average DTI parameter was extracted. The  
305 cluster-to-ROI conversion was done either directly if the cluster appeared well-delineated and  
306 confined to an anatomically discrete region e.g. Area X lesion detected by FA; or indirectly based on  
307 thresholded statistical maps ( $F$ -values) and anatomically recognizable areas e.g. the dorsal thalamic  
308 zone was extracted from peak  $F$ -values in the large cluster found in the SPM based on  $\lambda_1$ . The  
309 average DTI parameters were extracted for each individual cluster-based ROI and used for *post hoc*  
310 statistical testing to test when in time the differences occurred (Figure 4-B). For comparison, we  
311 extracted MRI parameters of a ROI in the caudomedial nidopallium which –to our knowledge– does  
312 not contain any connections to the Area X and is therefore hypothesized not to be affected by the  
313 lesion (Supplementary Figure S1).

314 Fractional anisotropy and  $\lambda_1$  showed an immediate increase in Area X (lesion site and caudal to  
315 lesion) at 2 weeks and further at 1 month *post-surgery*, after which they remained stable (Figure 4-B,  
316 FA for cluster (a)). At the needle penetration area, FA and  $\lambda_1$  values increased acutely at 2 weeks  
317 *post-surgery* due to the penetration and remained stable from 2 weeks onwards (Figure 4-B, FA for  
318 cluster (b)). The changes in MD and  $\lambda_1$  observed in the dorsal thalamic zone (including DLM)  
319 occurred more gradually. From baseline towards 1 month after surgery, MD and  $\lambda_1$  decreased slowly,  
320 yet, from 1 to 2 months *post-surgery* both DTI metrics increased significantly and remained relatively  
321 constant thereafter (Figure 4-B, MD for cluster (c)). The lateral cerebellar nuclei (Figure 4-B,  $\lambda_1$  for  
322 cluster (d)), tOM (Figure 4-B, MD for cluster (e)), and the *commissura posterior* (Figure 4-B,  $\lambda_1$  for  
323 cluster (f)) follow similar trends over time, i.e. a decrease at 2 weeks and 1 month after which they  
324 return to baseline levels at 2 or 3 months *post-surgery* and remain stable until the end of the study.



325

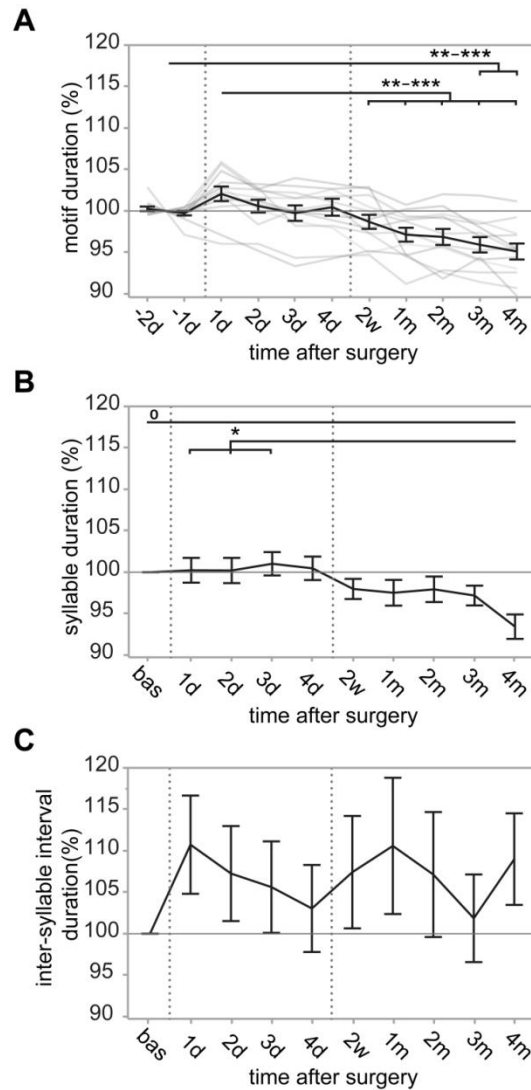
**Figure 4: DTI detects microstructural remodeling in the cerebello-thalamo-basal ganglia pathway.** **A:** The statistical parametric maps display the main effect of time derived from a repeated-measures ANOVA ( $n=12$ ), for FA, MD (at two different locations) and  $\lambda_1$ . The maps are thresholded at  $p_{FWE} < 0.05$  and  $k_E \geq 10$  voxels (F-values are color-coded according to the scales left to the SPMs), and overlaid on the population-based template. The black area reflects the lesioned area. The white-dotted crosshairs converge in local maxima (F-test), the latter of which have been the basis for drawing the cluster-based ROIs, appointed by (encircled) letters, i.e. (a): Area X (lesion); (b): entry of the needle; (c): dorsal thalamic zone; (d): lateral cerebellar nuclei; (e): tOM near the thalamus; and (f): commissura posterior. **B:** The bar graphs that illustrate the mean  $\pm$  standard deviation FA, MD and  $\lambda_1$  for several cluster-based ROIs identified in the voxel-wise statistical maps. The white letters at the base of the bars represent the results of the *post hoc* tests (Tukey HSD); if two time points share the same letter, then no significant difference exists between both. Each grey line presents the average DTI metric of the cluster for an individual bird over time. Time point '0' refers to the baseline, before neurotoxic lesioning. Abbreviations: Ro: rostral; Ca: caudal; Ve: ventral; Do: dorsal; L: left; R: right.

326 **3.4 Song motif duration acutely increases and later decreases following neurotoxic lesioning of**  
327 **Area X**

328 Due to technical limitations, we were not able to obtain song data of the baseline measurement for  
329 two out of 12 birds. Consequently, all song analyses were performed on 10 birds.

330 Motif duration changed significantly over the course of the study (mixed model main effect of time:  
331  $p < 0.0001$   $F_{(10,86.0)} = 13.0585$ ; Figure 5-A). From 3 months *post-surgery* onwards, motif duration was  
332 significantly shorter compared to baseline performance. The long-term decrease in motif duration  
333 can be ascribed to a progressive shortening of the syllable duration (mixed model main effect of  
334 time:  $p = 0.0110$   $F_{(11,98.8)} = 2.4019$ ; Figure 5-B), while the inter-syllable interval duration did not change  
335 significantly over time (mixed model main effect of time:  $p = 0.9823$   $F_{(11,97.9)} = 0.3098$ ; Figure 5-C). The  
336 latter exhibited a slight non-significant increase in duration immediately following surgery which  
337 persisted over the entire course of the study. Although the relative changes in syllable duration were  
338 smaller than those of inter-syllable duration, the absolute change in the durations of the syllables  
339 were bigger than the absolute change in the durations of inter-syllable intervals (respectively  $111.35$   
340  $\pm 5.82$  ms vs.  $35.07 \pm 1.92$  ms, mean  $\pm$  SEM; baseline data).

341 On average, syllables decreased in duration several months after lesioning. However, not all syllables  
342 presented a similar trajectory over time, as reflected in the relatively large variation (error bars)  
343 observed after lesioning. To test whether different syllable types would be affected in a specific way  
344 after lesioning, we categorised all syllables in accordance with criteria published by Sturdy et al.  
345 (1999). An overview of the syllable categorisation can be found in Table S1. We did not observe any  
346 unreadable or high note syllables. Next, we tested for significant changes in syllable duration for  
347 each category and observed a main effect of time for slide notes ( $p = 0.0092$   $F_{(11,21.4)} = 3.2649$ ),  
348 combination notes ( $p = 0.0017$   $F_{(11,47.2)} = 3.3786$ ) and unclassifiable syllables ( $p < 0.0001$   $F_{(11,75.3)} = 5.4896$ ).  
349 In contrast, short slide or flat note syllables did not present a significant main effect of time  
350 (respectively  $p = 0.0562$   $F_{(11,78.8)} = 1.8695$  or  $p = 0.4462$   $F_{(11,44.0)} = 1.0193$ ).



351

**Figure 5: Motif length acutely increases and later decreases following neurotoxic lesioning of Area X.** Motif length (A), the syllable (B) and inter-syllable intervals (C) durations are expressed relative (%) to the average baseline performance. The data is presented as mean  $\pm$  standard error of the mean ( $n=10$ ). Each grey line in (A) refers to the evolution of the average relative motif length for an individual bird over time, while the black line presents that average across all animals. The dotted lines subdivide the graph into three distinct phases relative to the surgery: baseline (bas or -2 and -1 days), acute (1-4 days after surgery) and chronic (2 weeks and 1-4 months after surgery) phases. Asterisks indicate the results of the mixed model with *post hoc* Tukey HSD, i.e. o:  $p=0.06$ ; \*:  $0.05 > p > 0.01$ ; \*\*  $0.01 > p > 0.001$ ; \*\*\*  $p < 0.001$ . Note that all statistical analyses have been performed on the *absolute* averaged data. Abbreviations: d: day; w: week; m: month.

352 **3.5 Song performance correlates with the microstructural properties of distinct areas in the**  
 353 **songbird brain**

354 Besides testing for effects of Area X lesioning on motif duration over time, we performed additional  
 355 tests to investigate possible relationships between the birds' motif duration and microstructural  
 356 tissue properties characterizing particular brain regions ( $n=10$ ). No significant clusters could be  
 357 observed in the voxel-wise multiple regression between smoothed (log-transformed) jacobian  
 358 determinant maps and motif duration, or for searching correlations between the jacobian

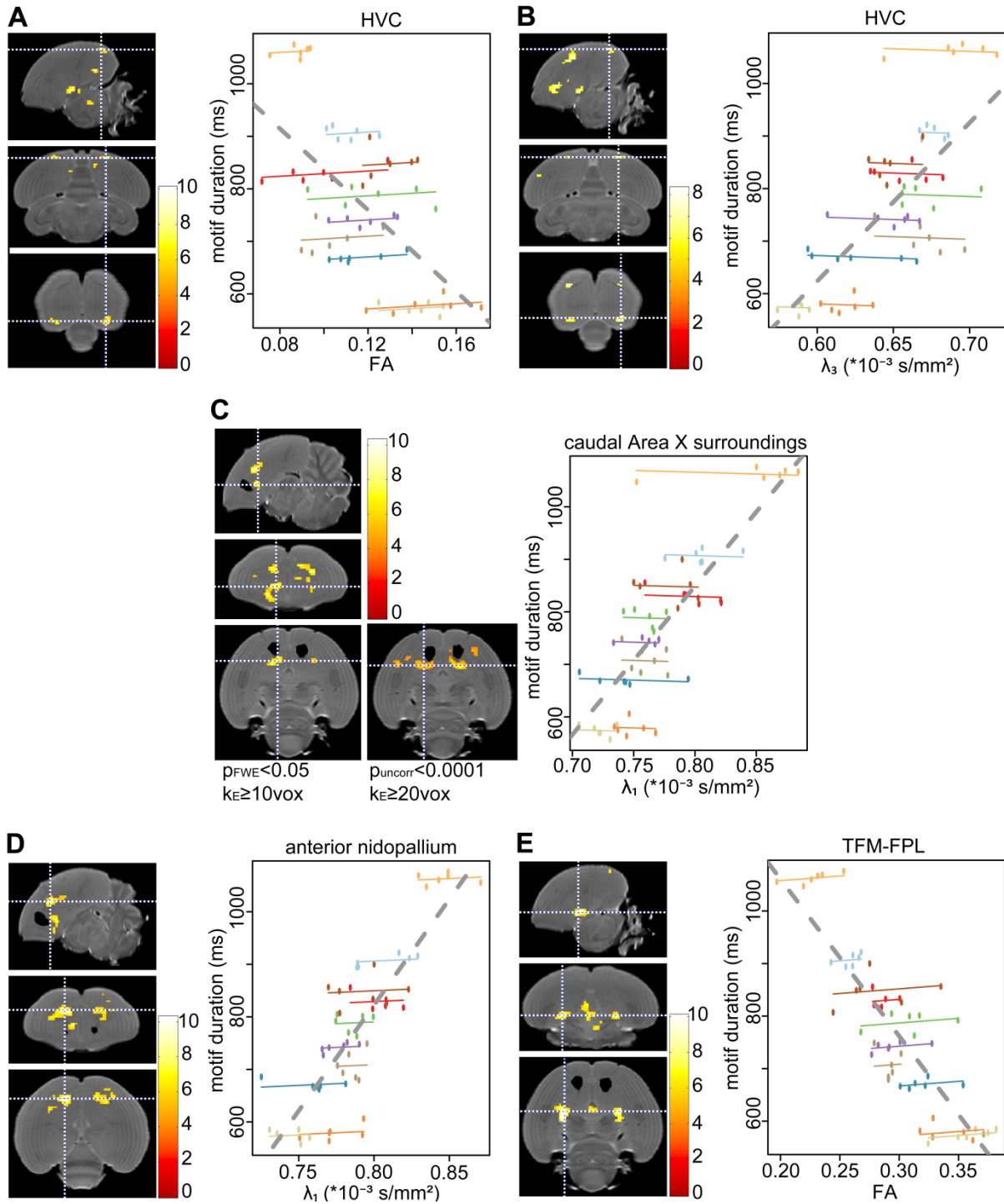
359 determinant or the DTI parameter maps and motif duration expressed relative to baseline. In  
360 contrast, several clusters displayed a correlation between motif duration and the smoothed DTI  
361 parameter maps. These clusters were converted to ROIs (cluster-based ROIs). Important to note is  
362 that the voxel-wise multiple regression does not take bird-identity into account; it describes the  
363 overall association between the song performance and a specific MRI parameter. Consequently, to  
364 find out whether the correlations detected by voxel-wise statistical testing were mainly driven by  
365 within- or between-bird variance, we performed a repeated-measures correlation analysis on the  
366 cluster-based ROI data (Bakdash and Marusich 2017). Figure 6 informs on the spatial location of the  
367 observed clusters (voxel-wise multiple regression) and the adjacent graphs illustrate the nature of  
368 the within- and between-subject correlation (Bakdash and Marusich 2017). Table 1 summarizes the  
369 cluster size, peak and cluster  $p$ -values, overall data association (Spearman's  $\rho$ ) and within-subject  
370 correlation (rmcorr) and corresponding  $p$ -value of the repeated-measures correlation analyses of the  
371 cluster-based ROIs.

372 A negative correlation between FA and motif duration was found near the ventro-rostral border of  
373 HVC and/or HVC<sub>shelf</sub> (Figure 6-A) and was mirrored by a positive correlation between motif duration  
374 and  $\lambda_2$  (data not shown) and  $\lambda_3$  (Figure 6-B). Furthermore, a positive correlation between motif  
375 duration and  $\lambda_1$ , and motif duration and MD was identified in the caudal parts of the striatum  
376 immediately adjacent to (but not co-localizing with) the lesion (Figure 6-C). At a milder statistical  
377 threshold ( $p_{\text{uncorrected}} < 0.0001$   $k_E \geq 20$  voxels), the cluster extends more laterally and appears more  
378 symmetric and comparable in size between both hemispheres (Figure 6-C, horizontal right). In  
379 addition,  $\lambda_1$  (and MD) correlated positively with motif duration in the anterior nidopallium dorsal to  
380 and potentially including parts of LMAN (Figure 6-D). Lastly, a negative correlation between FA and  
381 motif duration was found near a white matter structure which was identified as the *fasciculus*  
382 *prosencephalis lateralis* (FPL; according to (Karten et al. 2013)) or a white matter structure  
383 containing both the FPL and the *tractus thalamo-frontalis et frontalis thalamicus medialis* (TFM;  
384 based on (Nixdorf-Bergweiler and Bischof 2007); Figure 6-E). Interestingly, a similar cluster was  
385 found to display a positive correlation between  $\lambda_3$  and motif duration (data not shown). MD resulted  
386 in a similar statistical parametric map as  $\lambda_1$  when correlating with motif duration (results not shown).

**Table 1: Summary of the correlation analyses (n=10).**

Cluster-based ROI	DTI parameter	Hemis- phere	Cluster level		Peak level		Overall association		rmcorr	
			$p_{FWE}$	$k_E$	$p_{FWE}$	$T$	Spearman's $\rho$	$p$	$r$	
TFM / LFP	FA	left	<0.001	78	<0.001	10.06	-0.8265	0.156	0.202	
		right	<0.001	44	<0.001	9.09	-0.7497	0.684	-0.058	
	$\lambda_3$	left	<0.001	510	<0.001	8.10*	0.7440	.	.	
		right	<0.001	32	0.001	6.45	0.6427	.	.	
HVC (and HVC <sub>shelf</sub> )	FA	left	<0.001	46	<0.001	7.05	-0.7828	0.698	-0.056	
		right	<0.001	10	<0.001	6.61	-0.5266	0.145	0.207	
	$\lambda_3$	left	<0.001	12	<0.001	7.74	0.5507	0.782	0.044	
		right	<0.001	24	<0.001	6.95	0.6691	0.450	-0.108	
Caudal surroundings of lesion	$\lambda_1$	left	<0.001	87	<0.001	8.66	0.7546	0.517	-0.093	
		right	<0.001	10	0.008	5.78	0.6078	0.009	0.361	
Anterior nidopallium dorsal to LMAN	MD	left	<0.001	601	<0.001	9.81*	0.7383	.	.	
		right	<0.001	447	<0.001	7.40*	0.6836	.	.	
	$\lambda_1$	left	<0.001	141	<0.001	10.28	0.7859	0.443	0.110	
		right	<0.001	160	<0.001	8.10	0.7245	0.952	0.009	

\*This is the T-max of a sub-peak co-localized with the anatomical area delineated by the cluster-based ROI. The spatial extent of the cluster is not necessarily constricted to the anatomical area, but can be co-localized with the brain region to which the cluster-based ROI refers. Several subpeaks within the same cluster can be assigned to different cluster-based ROIs e.g. caudal surroundings of the lesion and anterior nidopallium dorsal to LMAN. Spearman's  $\rho$  is calculated based on all data of all time points and describes the overall association between the DTI parameter and motif duration, without taking bird-identity into account. 'rmcorr' refers to the outcome of the repeated-measures correlation with the average within-subject correlation coefficient 'r' and the corresponding p-value 'p' (Bakdash and Marusich 2017).



387

**Figure 6: Voxel-wise correlations between motif length and DTI metrics.** The crosshairs (white dotted lines) converge in (A-B) HVC and/or HVC<sub>shelf</sub>, (C) medial striatum caudal to the lesion, (D) anterior nidopallium dorsal to LMAN, and (E) parts of the FPL and/or TFM. The statistical maps present the voxel-wise multiple regression ( $n=10$ ) between motif length (y-axis) and the DTI parameters (x-axis) on the graph immediately right to the SPMs. The statistical maps are displayed corrected for multiple comparisons using  $p_{FWE}<0.05$ , and  $k_E \geq 10$  voxels and T-values are color-coded according to the scales immediately right to the statistical maps. The black area reflects the lesioned area. The graphs are generated using ‘rmcorr’ (Bakdash and Marusich 2017) and visualize the common within-subject regression slope shared among individuals (colored lines) and overall relationship between motif length and the DTI parameter of the cluster-based ROIs (grey dashed line). Each color refers to an individual bird and each dot is an individual data point (6 times points per bird, presenting data of

the cluster-based ROI of one hemisphere as indicated in the adjacent SPM). Abbreviations: Do: dorsal; Ve: ventral; Ro: rostral; Ca: caudal; L: left; R: right.

## 388 **4 DISCUSSION**

389 The present study explored neuroplastic events, i.e. relative volume changes and alterations in  
390 microstructural tissue properties, that characterize both short- and long-term effects of neurotoxic  
391 lesioning of the striatal component of the song control circuitry in adult male zebra finches. We  
392 identified relative volume changes in an area immediately adjacent to the lesion site, and detected  
393 altered microstructural tissue properties in the lesion, the efferent dorsal thalamic zone (including  
394 DLM) and surprisingly also in the lateral cerebellar nuclei. Furthermore, as the neurotoxic injury was  
395 previously found to induce particular changes in vocal behavior (Kubikova et al. 2014; Lukacova et al.  
396 2016), we tested whether brain-behavior relationships could be established between motif duration  
397 and the structural properties of specific brain areas. This analysis revealed correlations between the  
398 DTI metrics and motif duration in several areas of which most could be linked to the C-BG-T-C loop  
399 involved in song maintenance.

### 400 **4.1 Striatal regeneration**

401 We observed relative volume changes taking place within the first two weeks after surgery including  
402 exclusively the medial and caudal striatal surroundings of the lesion site. The cluster partially co-  
403 localizes with the ventral pallidum which receives direct projections from Area X (Gale, Person, and  
404 Perkel 2008; Person et al. 2008). Ibotenic acid causes neuronal cell death by over-excitation, while  
405 keeping the surrounding tissue –extracellular matrix and passing nerve terminals from extrinsic  
406 origin– unaffected (Schwarcz et al. 1979). Its neurotoxic effect is fully exerted within 48h (Schwarcz  
407 et al. 1979) and leads to massive apoptosis in the lesioned area (Kubikova et al. 2014). Likewise, 2  
408 weeks after surgery, we did not observe any traces of altered image intensities remote to the path  
409 of the needle and Area X lesion site that might affect the spatial registration procedure. This  
410 suggests that the observed cluster is not a processing-related artifact.

411 The timing of the observed relative volume changes clearly aligns with our previous studies that  
412 described drastic neuroplastic processes occurring in the striatum within the first months after  
413 lesioning. More specifically, based on T2-weighted scans, (Lukacova et al. 2017) describe that the  
414 relative portion of Area X affected by the lesion decreased from 87% to 35% within the first month,  
415 to 20% at 3 months and 12% at 6 months after lesioning . Similarly, based on histology (Hu stain for  
416 neurons), (Kubikova et al. 2014) describe a drastic reduction in the lesion size after 2 weeks and 1  
417 month *post-surgery* accompanied with an increased number of proliferated cells (BrdU<sup>+</sup>) in the  
418 lesion and in the medial and lateral striatal lesion-surroundings. Moreover, this was paralleled by  
419 increasing numbers of functionally active and undirected singing-induced immediate early gene (IEG)

420 egr-1 expressing cells dispersed throughout the previously damaged Area X. In addition, several  
421 studies in adult zebra finches provide evidence that neural progenitor cells reach the striatum from  
422 the ventricular zone at its caudal and medial border, migrate to Area X, and are able to differentiate  
423 into medium spiny neurons (Scott and Lois 2007; Kosubek-Langer, Schulze, and Scharff 2017). All this  
424 indicates that new cells migrate from the ventricular zone adjacent to the striatum to the damaged  
425 area and transform into functionally-active medium spiny neurons. We argue that the relative  
426 volume changes that exclusively affect the caudo-medio-lateral lesion-surroundings might arise from  
427 massive regenerative neuroplastic processes taking place most extensively in the first month after  
428 neurotoxic lesioning.

#### 429 **4.2 Microstructural remodeling in the C-BG-T-C loop and cerebello-thalamic-striatal pathway**

430 One of the major aims of this experiment was to uncover possible remote brain regions displaying  
431 disparate microstructural tissue properties at different stages following neurotoxic injury. We  
432 observed subtle changes in diffusion properties in the dorsal thalamic zone (containing DLM).  
433 Structural alterations to the thalamus agree with data obtained by (Luo and Perkel 1999) who  
434 discovered a marked reduction of GABAergic nerve terminals of projection neurons originating from  
435 Area X in DLM 3-4 days after injecting ibotenic acid unilaterally in Area X of adult male zebra finches.  
436 Interestingly, our data suggest that the structural properties of the dorsal thalamic zone appear to  
437 normalize to baseline levels by 2 months *post-surgery* and remain constant thereafter. This might  
438 imply a reinstatement of previously lost connectivity.

439 Within the first month after surgery, we observed significantly deviating  $\lambda_1$  in a bilateral cluster in  
440 the cerebellum covering the lateral portion of the deep nuclei. Tract tracing experiments in zebra  
441 finches (Person et al. 2008), canaries (Vates, Vicario, and Nottebohm 1997) and pigeons (Arends and  
442 Zeigler 1991) describe a di-synaptic connection between the cerebellum and the contralateral  
443 medial striatum and Area X. More specifically, they observed a coextensive stain within the dorsal  
444 thalamic zone when injecting retrograde tracers in Area X and the medial striatum and anterograde  
445 tracer in the contralateral cerebellum. Positively stained nerve terminals in the dorsal thalamic zone  
446 included the dorsomedial anterior and posterior nucleus of the thalamus (respectively DMA and  
447 DMP), but merely surrounded DLM (Vates, Vicario, and Nottebohm 1997), suggesting that cerebellar  
448 input to the contralateral Area X is indirect and relayed via the thalamus. In humans, it is well known  
449 that the cerebellum connects to the basal ganglia and takes an important part in both speech  
450 acquisition in early childhood and feedforward motor input in adulthood (for review (Ziegler and  
451 Ackermann 2017)). As such, the basal ganglia serve as a 'platform' where the cerebro-striatal and  
452 cerebellar pathways converge (Ziegler and Ackermann 2017). Our findings clearly point to a potential  
453 avian analogue of the feedforward cerebellar connection observed in humans. Further research is

454 required to unravel the distinct functional roles of each pathway in vocal motor control and to  
455 explore potential parallels between songbirds and humans.

### 456 **4.3 Striatal lesion affects motif duration**

457 Area X lesioning after song crystallization has little effect on the overall structure of the song (Scharff  
458 and Nottebohm 1991). More recent research (Kubikova et al. 2014; Lukacova et al. 2016) as well as  
459 this study showed a gradual decrease in motif duration reaching approximately 95% relative to  
460 baseline duration at 4 months after surgery. Interestingly, reduced syllable duration with intact song  
461 structure points to alterations in song tempo: birds progressively appeared to sing faster compared  
462 to baseline performance. Similarly, patient studies have reported that even though the sound  
463 structure of vocal utterances remains unaffected, dysarthric patients with striatal disorders or  
464 cerebellar abnormalities exhibited normal, slowed or accelerated speech rates (Bodranghien et al.  
465 2016; Riecker et al. 2006). The relatively divergent disease phenotypes underlying basal ganglia  
466 dysfunctioning underscore that more research is needed to unravel the pathophysiological role of  
467 each component in vocal motor output.

468 We observed several correlations between local diffusion properties and motif duration, including  
469 clusters in/near HVC, the caudo-medio-lateral striatal surroundings of the lesion site, the TFM/LFP,  
470 and the anterior nidopallium (cortical) dorsal to LMAN<sub>core/shell</sub>. These are brain areas linked to the C-  
471 BG-T-C pathways in control of song behavior. Important to note is that **all** of the areas identified by  
472 the voxel-based analysis are driven by variability in motif duration present between birds, rather  
473 than variation in motif duration as a consequence of the striatal injury (visible in correlation graphs  
474 in Figure 6; Table 1).

#### 475 **4.3.1 Motif duration & HVC**

476 HVC sends direct projections to Area X (Nottebohm, Stokes, and Leonard 1976). Even though no  
477 direct microstructural changes in HVC could be observed along the course of the study, it might be  
478 plausible that the correlation between FA or  $\lambda_3$  with motif duration might in part be driven by direct  
479 lesion-induced structural remodeling propagating upstream, to HVC.

480 Across songbird species, brain-behavior relationships have been observed between the volume or  
481 cell number of song control system components and song performance. Indeed, HVC volume  
482 correlates positively with the number of syllables in the song of male canaries (Nottebohm,  
483 Kasparian, and Pandazis 1981) or with song repertoire size in Marsh wrens (Canady, Kroodsma, and  
484 Nottebohm 1984), song sparrows (Pfaff et al. 2007), and in warblers (Székely et al. 1996; Airey et al.  
485 2000). In male zebra finches, HVC volume and neuron number correlates positively with the number  
486 of tutor syllables that are accurately copied (Ward, Nordeen, and Nordeen 1998; Airey and DeVoogd

487 2000). Likewise, the correlation observed between FA or  $\lambda_3$  and motif length might in part rely on a  
488 potential volume difference between HVC of birds singing short compared to longer song motifs,  
489 that might still remain present after the spatial normalization procedure.

490 Alternatively, substantial evidence has appointed HVC as time keeper of song, i.e. HVC is involved in  
491 control of the temporal characteristics of the motor program underlying a particular song  
492 (Hahnloser, Kozhevnikov, and Fee 2002; Ali et al. 2013). For example, both in humans and songbirds,  
493 localized cooling of respectively Broca's area or HVC affects speech rate or slows down song speed  
494 by stretching the motif sequence (Long and Fee 2008; Long et al. 2016). Even though the lesion-  
495 induced alterations in motif duration (song tempo) are not sufficient to result in clear within-subject  
496 correlations, part of the correlation might build on subtle differences in song tempo controlled by  
497 HVC.

#### 498 **4.3.2 Motif duration & TFM/LFP & caudal surroundings of the lesion**

499 The voxel-based multiple regression demonstrated clear bilateral clusters in a part of the TFM/FPL  
500 (motif duration correlated negatively with FA and positively with  $\lambda_3$ ) and the caudal surroundings of  
501 the lesion (motif duration correlated positively with  $\lambda_1$  and MD). The latter one was found to display  
502 relative volume changes within 1 month *post-surgery*.

503 The TFM/FPL is a white matter tract that accommodates fibers pertaining to the striato-thalamic  
504 part of the AFP. More specifically, after exiting Area X from its caudo-ventral end, Area X projection  
505 neurons course to the region of the FPL and TFM, infiltrate DLM via its anterior part where the axon  
506 terminals form a basket-like lattice surrounding DLM cells (Luo and Perkel 1999; Bottjer et al. 1989;  
507 Person et al. 2008).

508 Previous studies have shown that undirected singing-driven IEG *egr-1* expression levels in RA are  
509 dependent on Area X and a functioning AFP (Kubikova, Turner, and Jarvis 2007). Intriguingly, upon  
510 neurotoxic lesioning of Area X, undirected singing-driven *egr-1* expression levels drop and only  
511 recover between 1-3 months after Area X lesioning (Kubikova et al. 2014). Consequently, the lack of  
512 expression of IEG *egr-1* in RA suggests that the AFP is not yet fully functional before 1 month after  
513 neurotoxic damage to Area X. Similarly, partial lesioning of Area X lowers the undirected singing-  
514 driven IEG expression in the intact Area X (Kubikova, Turner, and Jarvis 2007). This might be due to  
515 altered local interconnectivity within the striatum as, in normal circumstances, striatal neurons are  
516 tightly interconnected (Reiner, Laverghetta, et al. 2004). Together with the previously reported  
517 massive regenerative processes (Kubikova et al. 2014) that coincide and co-localize with the relative  
518 volume differences observed in this study, the voxel-wise correlations between the DTI metrics and  
519 motif length might connect tissue remodeling aimed at recovering local connectivity within Area X

520 but also with the neighboring striatum and downstream AFP to alterations in vocal performance.  
521 Therefore, our findings align with Kubikova et al. (2014) who hypothesized that behavioral changes  
522 might be a direct result of new neurons being integrated to re-establish connectivity locally and  
523 within the AFP after Area X lesioning.

#### 524 **4.3.3 Motif duration & anterior nidopallium and/or LMAN<sub>shell/core</sub>**

525 When searching for possible correlations between DTI metrics and motif duration, we discovered a  
526 clear bilateral cluster near the anterior nidopallium dorsal to (and potentially including parts of)  
527 LMAN<sub>core/shell</sub>. We propose two explanations underlying this observation: (1) this region might be  
528 directly affected by the surgical procedure and/or back flow of ibotenic acid, or directly by lesioning  
529 of Area X, or (2) this finding might point to involvement of the parallel AFP.

#### 530 **Surgical procedure or direct effect by neurotoxic lesioning**

531 Based on the T<sub>2</sub>-weighted scans acquired 2 days after the surgery, we concluded that the anterior  
532 nidopallium possibly including a small rostral portion of the LMAN<sub>core/shell</sub> might be covered by edema  
533 (Figure 2) and thus affected by either mechanical or neurotoxic damage. The latter is not very likely,  
534 as based on effects over time, we did not observe clear clusters co-localized with the caudal  
535 nidopallium nor LMAN that could indicate microstructural remodeling due to a lesion. The only  
536 cluster covering the anterior nidopallium possibly involving parts of LMAN<sub>core/shell</sub> was found when  
537 testing for a correlation with motif duration, the latter of which appeared to change over time.  
538 Alternatively, LMAN sends a direct projection back to Area X (Vates and Nottebohm 1995; Nixdorf-  
539 Bergweiler, Lips, and Heinemann 1995). Consequently, the cluster that partly overlaps with LMAN  
540 might suggest direct lesion-induced structural alterations affecting one of its immediate up-stream  
541 areas. As singing-induced *egr-1* expression in LMAN is reduced after Area X lesions (Kubikova,  
542 Turner, and Jarvis 2007), this again suggests a direct effect of lesioning.

#### 543 **Parallel pathways**

544 When mapping the thalamo-cortical part of the AFP, i.e. DLM-LMAN-RA pathway, in adult male  
545 zebra finches, Johnson and co-workers provided evidence for two parallel pathways originating in  
546 different sub-regions of DLM (Johnson, Sablan, and Bottjer 1995). One set emerged from the  
547 dorsolateral portion of DLM, connected with the LMAN<sub>core</sub> and ended in RA. The other pathway  
548 included axonal projections stemming from the medioventral portion of DLM, projected to the  
549 LMAN<sub>shell</sub> region and travelled further to the dorsal arcopallium (arc-like structure within the  
550 arcopallium lateral to RA). Follow-up studies showed that the LMAN<sub>shell</sub> also projects to ventral parts  
551 of the arcopallium and the dorsal caudolateral nidopallium, and receives connections from the  
552 contralateral ventral arcopallium, recently summarized by (Paterson and Bottjer 2017). Moreover,  
553 disruption of the LMAN<sub>shell</sub> circuitry (by lesioning the dorsal arcopallium) during the critical period of

554 vocal learning prevents birds from imitating an accurate copy of the tutor song (Bottjer and Altenau  
555 2010). Based on these and other findings, the LMAN<sub>shell</sub> region might serve as entry site for  
556 multimodal sensory information (inputted via the dorsal caudolateral nidopallium) in the song  
557 control system and might be implicated in the bilateral coordination of the song control circuitries  
558 situated in the left and right hemispheres (Paterson and Bottjer 2017). Yet, the exact role of the  
559 parallel pathway on vocal behavior requires further investigation.

## 560 **5 CONCLUSION**

561 Using whole-brain *in vivo* structural MRI including DTI and 3D anatomical scans combined with voxel-  
562 wise statistical testing, this study complements previous reports on the detection of microstructural  
563 remodeling following neurotoxic lesioning of Area X in brain sites reaching as far as the cerebellum.  
564 This finding calls out the need for in-depth studies focused on the role of the lateral cerebellar nuclei  
565 in song learning in ontogeny, and extends existing parallels between bird song and human speech  
566 (Brainard and Doupe 2013; Ziegler and Ackermann 2017). As such, songbirds might help resolve the  
567 open questions concerning the physiological workings and interplay of the cortical and subcortical  
568 neural network architecture that underlies speech motor production which is of vital importance to  
569 understand how proper speech control is altered in various disorders of the human brain.

## **FUNDING**

This work was supported by grants from the Research Foundation—Flanders (FWO, Project No. G030213N, G044311N and G037813N), the Hercules Foundation (Grant No. AUHA0012), Interuniversity Attraction Poles (IAP) initiated by the Belgian Science Policy Office ('PLASTOSCINE': P7/17 and P7/11) to AVdL, and a grant from the Slovak Research and Development Agency (APVV-15-0077) to LK. JH is a PhD student supported by the University of Antwerp.

## **ACKNOWLEDGEMENTS**

The computational resources and services used in this work to build the population-based template were provided by the HPC core facility CalcUA of the Universiteit Antwerpen, the VSC (Flemish Supercomputer Center), funded by the Hercules Foundation and the Flemish Government – department EWI. We thank prof. Dr. E. Fransen (StatUa Center for Statistics) for a critical revision of the statistical methodology (mixed models). We also thank Dr. Erich D. Jarvis for his insights and advice at localizing brain areas.

570 **REFERENCES**

- 571 Airey, David C., Katherine L. Buchanan, Tamas Szekely, Clive K. Catchpole, and Timothy J. DeVoogd.  
572 2000. 'Song, sexual selection, and a song control nucleus (HVC) in the brains of European sedge  
573 warblers', *Journal of Neurobiology*, 44: 1-6.
- 574 Airey, David C., and Timothy J. DeVoogd. 2000. 'Greater song complexity is associated with  
575 augmented song system anatomy in zebra finches', *NeuroReport*, 11: 2339-44.
- 576 Ali, Farhan, Timothy M. Otchy, Cengiz Pehlevan, Antoniu L. Fantana, Yoram Burak, and Bence P.  
577 Ölveczky. 2013. 'The basal ganglia is necessary for learning spectral, but not temporal features of  
578 birdsong', *Neuron*, 80: 494-506.
- 579 Arends, J. J. A., and H. Philip Zeigler. 1991. 'Organization of the cerebellum in the pigeon (*Columba*  
580 *livia*): II. Projections of the cerebellar nuclei', *The Journal of Comparative Neurology*, 306: 245-72.
- 581 Ashburner, J., and G. R. Ridgway. 2015. 'Tensor-Based Morphometry A2 - Toga, Arthur W.' in, *Brain*  
582 *Mapping* (Academic Press: Waltham).
- 583 Ashburner, John. 2007. 'A fast diffeomorphic image registration algorithm', *NeuroImage*, 38: 95-113.
- 584 Ashburner, John, and Karl J. Friston. 2009. 'Computing average shaped tissue probability templates',  
585 *NeuroImage*, 45: 333-41.
- 586 Ashburner, John, and Gerard R. Ridgway. 2012. 'Symmetric Diffeomorphic Modeling of Longitudinal  
587 Structural MRI', *Frontiers in Neuroscience*, 6: 197.
- 588 Avants, B. B., C. L. Epstein, M. Grossman, and J. C. Gee. 2008. 'Symmetric diffeomorphic image  
589 registration with cross-correlation: Evaluating automated labeling of elderly and  
590 neurodegenerative brain', *Medical Image Analysis*, 12: 26-41.
- 591 Avants, Brian B., Nicholas J. Tustison, Gang Song, Philip A. Cook, Arno Klein, and James C. Gee. 2011.  
592 'A reproducible evaluation of ANTs similarity metric performance in brain image registration',  
593 *NeuroImage*, 54: 2033-44.

594 Avants, Brian B., Paul Yushkevich, John Pluta, David Minkoff, Marc Korczykowski, John Detre, and  
595 James C. Gee. 2010. 'The optimal template effect in hippocampus studies of diseased  
596 populations', *NeuroImage*, 49: 2457-66.

597 Bakdash, Jonathan Z., and Laura R. Marusich. 2017. 'Repeated Measures Correlation', *Frontiers in*  
598 *Psychology*, 8: 456.

599 Bodranghien, Florian, Amy Bastian, Carlo Casali, Mark Hallett, Elan D. Louis, Mario Manto, Peter  
600 Mariën, Dennis A. Nowak, Jeremy D. Schmahmann, Mariano Serrao, Katharina Marie Steiner,  
601 Michael Strupp, Caroline Tilikete, Dagmar Timmann, and Kim van Dun. 2016. 'Consensus Paper:  
602 Revisiting the Symptoms and Signs of Cerebellar Syndrome', *The Cerebellum*, 15: 369-91.

603 Bolhuis, Johan J., Kazuo Okanoya, and Constance Scharff. 2010. 'Twitter evolution: converging  
604 mechanisms in birdsong and human speech', *Nat Rev Neurosci*, 11: 747-59.

605 Bottjer, Sarah W., and Brie Altenau. 2010. 'Parallel pathways for vocal learning in basal ganglia of  
606 songbirds', *Nat Neurosci*, 13: 153-55.

607 Bottjer, Sarah W., Keri A. Halsema, Sandra A. Brown, and Elizabeth A. Miesner. 1989. 'Axonal  
608 connections of a forebrain nucleus involved with vocal learning in zebra finches', *The Journal of*  
609 *Comparative Neurology*, 279: 312-26.

610 Brainard, Michael S. 2004. 'Contributions of the Anterior Forebrain Pathway to Vocal Plasticity',  
611 *Annals of the New York Academy of Sciences*, 1016: 377-94.

612 Brainard, Michael S., and Allison J. Doupe. 2013. 'Translating Birdsong: Songbirds as a Model for  
613 Basic and Applied Medical Research', *Annual Review of Neuroscience*, 36: 489-517.

614 Canady, R A, D E Kroodsma, and F Nottebohm. 1984. 'Population differences in complexity of a  
615 learned skill are correlated with the brain space involved', *Proceedings of the National Academy*  
616 *of Sciences*, 81: 6232-34.

617 Doetsch, F., and C. Scharff. 2001. 'Challenges for Brain Repair: Insights from Adult Neurogenesis in  
618 Birds and Mammals', *Brain, Behavior and Evolution*, 58: 306-22.

619 Doupe, Allison J., David J. Perkel, Anton Reiner, and Edward A. Stern. 2005. 'Birdbrains could teach  
620 basal ganglia research a new song', *Trends in Neurosciences*, 28: 353-63.

621 Ernst, Aurélie, Kanar Alkass, Samuel Bernard, Mehran Salehpour, Shira Perl, John Tisdale, Göran  
622 Possnert, Henrik Druid, and Jonas Frisé. 'Neurogenesis in the Striatum of the Adult Human  
623 Brain', *Cell*, 156: 1072-83.

624 Gale, Samuel D., Abigail L. Person, and David J. Perkel. 2008. 'A novel basal ganglia pathway forms a  
625 loop linking a vocal learning circuit with its dopaminergic input', *The Journal of Comparative  
626 Neurology*, 508: 824-39.

627 Glaze, Christopher M., and Todd W. Troyer. 2006. 'Temporal Structure in Zebra Finch Song:  
628 Implications for Motor Coding', *The Journal of Neuroscience*, 26: 991-1005.

629 Goldman, S A, and F Nottebohm. 1983. 'Neuronal production, migration, and differentiation in a  
630 vocal control nucleus of the adult female canary brain', *Proceedings of the National Academy of  
631 Sciences*, 80: 2390-94.

632 Hahnloser, Richard H. R., Alexay A. Kozhevnikov, and Michale S. Fee. 2002. 'An ultra-sparse code  
633 underlies the generation of neural sequences in a songbird', *Nature*, 419: 65-70.

634 Hamaide, Julie, Geert De Groof, Gwendolyn Van Steenkiste, Ben Jeurissen, Johan Van Audekerke,  
635 Maarten Naeyaert, Lisbeth Van Ruijssevelt, Charlotte Cornil, Jan Sijbers, Marleen Verhoye, and  
636 Annemie Van der Linden. 2017. 'Exploring sex differences in the adult zebra finch brain: In vivo  
637 diffusion tensor imaging and ex vivo super-resolution track density imaging', *NeuroImage*, 146:  
638 789-803.

639 Jarvis, Erich D. 2004. 'Learned Birdsong and the Neurobiology of Human Language', *Annals of the  
640 New York Academy of Sciences*, 1016: 749-77.

641 Jarvis, Erich D., Onur Gunturkun, Laura Bruce, Andras Csillag, Harvey Karten, Wayne Kuenzel, Loreta  
642 Medina, George Paxinos, David J. Perkel, Toru Shimizu, Georg Striedter, J. Martin Wild, Gregory F.  
643 Ball, Jennifer Dugas-Ford, Sarah E. Durand, Gerald E. Hough, Scott Husband, Lubica Kubikova,  
644 Diane W. Lee, Claudio V. Mello, Alice Powers, Connie Siang, Tom V. Smulders, Kazuhiro Wada,

645 Stephanie A. White, Keiko Yamamoto, Jing Yu, Anton Reiner, and Ann B. Butler. 2005. 'Avian  
646 brains and a new understanding of vertebrate brain evolution', *Nat Rev Neurosci*, 6: 151-59.

647 Johnson, Frank, Michelle M. Sablan, and Sarah W. Bottjer. 1995. 'Topographic organization of a  
648 forebrain pathway involved with vocal learning in zebra finches', *The Journal of Comparative  
649 Neurology*, 358: 260-78.

650 Karten, Harvey J., Agnieszka Brzozowska-Prechtl, Peter V. Lovell, Daniel D. Tang, Claudio V. Mello,  
651 Haibin Wang, and Partha P. Mitra. 2013. 'Digital Atlas of the Zebra Finch (*Taeniopygia guttata*)  
652 Brain: a High Resolution Photo Atlas', *The Journal of Comparative Neurology*, 521: 3702-15.

653 Kobayashi, Kohta, Hiroyuki Uno, and Kazuo Okanoya. 2001. 'Partial lesions in the anterior forebrain  
654 pathway affect song production in adult Bengalese finches', *NeuroReport*, 12: 353-58.

655 Kosubek-Langer, Jennifer, Lydia Schulze, and Constance Scharff. 2017. 'Maturation, Behavioral  
656 Activation, and Connectivity of Adult-Born Medium Spiny Neurons in a Striatal Song Nucleus',  
657 *Frontiers in Neuroscience*, 11.

658 Kubikova, Lubica, Eva Bosikova, Martina Cvikova, Kristina Lukacova, Constance Scharff, and Erich D.  
659 Jarvis. 2014. 'Basal ganglia function, stuttering, sequencing, and repair in adult songbirds',  
660 *Scientific Reports*, 4: 6590.

661 Kubikova, Lubica, Elena A. Turner, and Erich D. Jarvis. 2007. 'The pallial basal ganglia pathway  
662 modulates the behaviorally driven gene expression of the motor pathway', *The European Journal  
663 of Neuroscience*, 25: 2145-60.

664 Long, Michael A., and Michale S. Fee. 2008. 'Using temperature to analyse temporal dynamics in the  
665 songbird motor pathway', *Nature*, 456: 189-94.

666 Long, Michael A, Kalman A Katlowitz, Mario A Svirsky, Rachel C Clary, Tara McAllister Byun, Najib  
667 Majaj, Hiroyuki Oya, Matthew A Howard, and Jeremy D W. Greenlee. 2016. 'Functional  
668 Segregation of Cortical Regions Underlying Speech Timing and Articulation', *Neuron*, 89: 1187-93.

669 Lukacova, Kristina, Ladislav Baciak, Eva Pavukova, Katarina Pichova, Svatava Kasparova, and Lubica  
670 Kubikova. 2017. 'Imaging of striatal injury in a songbird brain', *General Physiology and Biophysics*,  
671 36: 5.

672 Lukacova, Kristina, Eva Pavukova, Lubor Kostal, Boris Bilcik, and Lubica Kubikova. 2016. 'Dopamine  
673 D3 receptors modulate the rate of neuronal recovery, cell recruitment in Area X, and song tempo  
674 after neurotoxic damage in songbirds', *Neuroscience*, 331: 158-68.

675 Luo, Minmin, and David J. Perkel. 1999. 'Long-range GABAergic projection in a circuit essential for  
676 vocal learning', *The Journal of Comparative Neurology*, 403: 68-84.

677 MacDougall-Shackleton, Scott A., and Gregory F. Ball. 1999. 'Comparative studies of sex differences  
678 in the song-control system of songbirds', *Trends in Neurosciences*, 22: 432-36.

679 Moorman, Sanne, Sharon M. H. Gobes, Maaïke Kuijpers, Amber Kerkhofs, Matthijs A. Zandbergen,  
680 and Johan J. Bolhuis. 2012. 'Human-like brain hemispheric dominance in birdsong learning',  
681 *Proceedings of the National Academy of Sciences*, 109: 12782-87.

682 Mori, Susumu, and Jiangyang Zhang. 2006. 'Principles of Diffusion Tensor Imaging and Its  
683 Applications to Basic Neuroscience Research', *Neuron*, 51: 527-39.

684 Nixdorf-Bergweiler, Barbara, and Hans-Joachim Bischof. 2007. *Atlas Of The Brain Of The Zebra Finch,*  
685 *Taeniopygia Guttata: With Special Emphasis On Telencephalic Visual And Song System Nuclei in*  
686 *Transverse and Sagittal Sections.*

687 Nixdorf-Bergweiler, Barbara E., Mario B. Lips, and Uwe Heinemann. 1995. 'Electrophysiological and  
688 morphological evidence for a new projection of LMAN-neurons towards area X', *NeuroReport*, 6:  
689 1729-32.

690 Nordeen, K. W., and E. J. Nordeen. 2010. 'Deafening-Induced Vocal Deterioration in Adult Songbirds  
691 Is Reversed by Disrupting a Basal Ganglia-Forebrain Circuit', *The Journal of Neuroscience*, 30:  
692 7392-400.

693 Nottebohm, F, and AP Arnold. 1976. 'Sexual dimorphism in vocal control areas of the songbird brain',  
694 *Science*, 194: 211-13.

695 Nottebohm, Fernando, Susan Kasparian, and Constantine Pandazis. 1981. 'Brain space for a learned  
696 task', *Brain Research*, 213: 99-109.

697 Nottebohm, Fernando, Tegner M. Stokes, and Christiana M. Leonard. 1976. 'Central control of song  
698 in the canary, *Serinus canarius*', *The Journal of Comparative Neurology*, 165: 457-86.

699 Paterson, Amy K., and Sarah W. Bottjer. 2017. 'Cortical inter-hemispheric circuits for multimodal  
700 vocal learning in songbirds', *Journal of Comparative Neurology*, 525: 3312-40.

701 Person, Abigail L., Samuel D. Gale, Michael A. Farries, and David J. Perkel. 2008. 'Organization of the  
702 songbird basal ganglia, including area X', *The Journal of Comparative Neurology*, 508: 840-66.

703 Petkov, Christopher I, and Erich Jarvis. 2012. 'Birds, Primates and Spoken Language Origins:  
704 Behavioral Phenotypes and Neurobiological Substrates', *Frontiers in Evolutionary Neuroscience*, 4.

705 Pfaff, Jeremy A, Liana Zanette, Scott A MacDougall-Shackleton, and Elizabeth A MacDougall-  
706 Shackleton. 2007. 'Song repertoire size varies with HVC volume and is indicative of male quality in  
707 song sparrows (*Melospiza melodia*)', *Proceedings of the Royal Society B: Biological*  
708 *Sciences*, 274: 2035-40.

709 Pfenning, Andreas R., Erina Hara, Osceola Whitney, Miriam V. Rivas, Rui Wang, Petra L. Roulhac,  
710 Jason T. Howard, Morgan Wirthlin, Peter V. Lovell, Ganeshkumar Ganapathy, Jacquelyn  
711 Mouncastle, M. Arthur Moseley, J. Will Thompson, Erik J. Soderblom, Atsushi Iriki, Masaki Kato,  
712 M. Thomas P. Gilbert, Guojie Zhang, Trygve Bakken, Angie Bongaarts, Amy Bernard, Ed Lein,  
713 Claudio V. Mello, Alexander J. Hartemink, and Erich D. Jarvis. 2014. 'Convergent transcriptional  
714 specializations in the brains of humans and song-learning birds', *Science (New York, N.Y.)*, 346:  
715 1256846-46.

716 Reiner, Anton, Antonio V. Laverghetta, Christopher A. Meade, Sherry L. Cuthbertson, and Sarah W.  
717 Bottjer. 2004. 'An immunohistochemical and pathway tracing study of the striatopallidal  
718 organization of area X in the male zebra finch', *The Journal of Comparative Neurology*, 469: 239-  
719 61.

720 Reiner, Anton, David J. Perkel, Claudio V. Mello, and Erich D. Jarvis. 2004. 'Songbirds and the Revised  
721 Avian Brain Nomenclature', *Annals of the New York Academy of Sciences*, 1016: 77-108.

722 Riecker, Axel, Jan Kassubek, Klaus Gröschel, Wolfgang Grodd, and Hermann Ackermann. 2006. 'The  
723 cerebral control of speech tempo: Opposite relationship between speaking rate and BOLD signal  
724 changes at striatal and cerebellar structures', *NeuroImage*, 29: 46-53.

725 Scharff, C, and F Nottebohm. 1991. 'A comparative study of the behavioral deficits following lesions  
726 of various parts of the zebra finch song system: implications for vocal learning', *The Journal of*  
727 *Neuroscience*, 11: 2896-913.

728 Schwarcz, R., T. Hökfelt, K. Fuxe, G. Jonsson, M. Goldstein, and L. Terenius. 1979. 'Ibotenic acid-  
729 induced neuronal degeneration: A morphological and neurochemical study', *Experimental Brain*  
730 *Research*, 37: 199-216.

731 Scott, Benjamin B., and Carlos Lois. 2007. 'Developmental origin and identity of song system neurons  
732 born during vocal learning in songbirds', *The Journal of Comparative Neurology*, 502: 202-14.

733 Sturdy, Christopher B., Leslie S. Phillmore, and Ronald G. Weisman. 1999. 'Note types, harmonic  
734 structure, and note order in the songs of zebra finches (*Taeniopygia guttata*)', *Journal of*  
735 *Comparative Psychology*, 113: 194-203.

736 Székely, T., C.K. Catchpole, A. Devoogd, Z. Marchl, and T. J. DeVoogd. 1996. 'Evolutionary changes in  
737 a song control area of the brain (HVC) are associated with evolutionary changes in song  
738 repertoire among European warblers (*Sylviidae*)', *Proceedings of the Royal Society of London.*  
739 *Series B: Biological Sciences*, 263: 607.

740 Tchernichovski, Ofer, Fernando Nottebohm, Ching Elizabeth Ho, Bijan Pesaran, and Partha Pratim  
741 Mitra. 2000. 'A procedure for an automated measurement of song similarity', *Animal Behaviour*,  
742 59: 1167-76.

743 Vates, G E, and F Nottebohm. 1995. 'Feedback circuitry within a song-learning pathway', *Proceedings*  
744 *of the National Academy of Sciences*, 92: 5139-43.

745 Vates, G. Edward, David S. Vicario, and Fernando Nottebohm. 1997. 'Reafferent thalamo-“cortical”  
746 loops in the song system of oscine songbirds', *The Journal of Comparative Neurology*, 380: 275-  
747 90.

748 Vicario, David S. 1991. 'Organization of the zebra finch song control system: Functional organization  
749 of outputs from nucleus robustus archistriatalis', *The Journal of Comparative Neurology*, 309:  
750 486-94.

751 Ward, B. C., E. J. Nordeen, and K. W. Nordeen. 1998. 'Individual variation in neuron number predicts  
752 differences in the propensity for avian vocal imitation', *Proceedings of the National Academy of*  
753 *Sciences*, 95: 1277-82.

754 Wild, J. Martin. 1993. 'Descending projections of the songbird nucleus robustus archistriatalis', *The*  
755 *Journal of Comparative Neurology*, 338: 225-41.

756 ———. 1997. 'Neural pathways for the control of birdsong production', *Journal of Neurobiology*, 33:  
757 653-70.

758 Ziegler, W., and H. Ackermann. 2017. 'Subcortical Contributions to Motor Speech: Phylogenetic,  
759 Developmental, Clinical', *Trends in Neurosciences*, 40: 458-68.

760